Impact of pH-shifting on multiscale structural anisotropy of high-moisture extrudates of soy proteins

Kuijpers, Sam A.; Garina, Ekaterina D.; Gobes, Martijn I.; Adel, Ruud den; Smith, Gregory N.; Sztucki, Michael; Hohlbein, Johannes; Bouwman, Wim G.; van Duynhoven, John P.M.; Terenzi, Camilla

DOI
10.1016/j.foodhyd.2025.111456

Publication date
2025

Document Version
Final published version

Published in
Food Hydrocolloids

Food Hydrocolloids 168 (2025) 111456

Contents lists available at ScienceDirect

Food Hydrocolloids

journal homepage: www.elsevier.com/locate/foodhyd

Impact of pH-shifting on multiscale structural anisotropy of high-moisture extrudates of soy proteins

Sam A. Kuijpers [a,1], Ekaterina D. Garina [b,1], Martijn I. Gobes [a], Ruud den Adel [c], Gregory N. Smith [d], Michael Sztucki [e], Johannes Hohlbein [a,f], Wim G. Bouwman [b], John P.M. van Duynhoven [a,c,*], Camilla Terenzi [a,**]

[a] Laboratory of Biophysics, Wageningen University & Research, Stippeneng 4, 6708 WE Wageningen, The Netherlands
[b] Department of Radiation Science and Technology, Delft University of Technology, Mekelweg 15, 2629 JB Delft, The Netherlands
[c] Unilever Global Foods Innovation Centre, Bronland 14, 6708 WH Wageningen, The Netherlands
[d] ISIS Neutron and Muon Source, Science and Technology Facilities Council, Rutherford Appleton Laboratory, Chilton, Oxon OX11 0QX, UK
[e] ESRF, The European Synchrotron Radiation Facility, 71 Avenue des Martyrs, CS40220, 38043 Grenoble Cedex 9, France
[f] Microscopy Research Facility, Wageningen University & Research, Stippeneng 4, 6708 WE Wageningen, The Netherlands

ARTICLE INFO

Dataset link: https://doi.org/10.5286/ISIS.E.RB2269101, https://doi.org/10.5281/zenodo.14002334

Keywords:
Soy proteins
Anisotropic structure
High-moisture extrusion
pH-shifting
Magnetic resonance imaging
Small angle scattering

ABSTRACT

High-moisture extrusion (HME) is a proven industrial food processing technique used to create textured plant-protein materials that can serve as alternatives for animal meat. The required multiscale anisotropic structure of the extrudate can be achieved by selecting suitable HME process conditions, as well as by pH-shifting. In this work, we explored pH-shifting via the water feed, which is an attractive industrially-scalable approach. Soy protein concentrate (SPC) was extruded on lab-scale and extrudates were characterized *ex situ*, from molecular to mm scale, using Diffuse Reflectance (DR), Magnetic Resonance Imaging (MRI), Small-Angle-Scattering of Neutrons (SANS) or X-rays (SAXS). pH-shifting had a non-monotonic effect on extrudate hardness and anisotropic structure at both sub-mm (MRI) and μm (DR) scale. At the sub-μm scale, SANS and SAXS data indicated that, at pH > pI, the radius of protein nano-aggregates monotonically increases, accompanied by a transition from particulate to fibrillar protein aggregation. When pH was further shifted to alkaline conditions, the decrease in clustering strength and nematic order parameter pointed to an increase in intra- and inter-fibrillar repulsion, respectively. Protein extractability experiments indicated that the effects of pH-shifting on anisotropic structure formation could not be attributed to covalent intermolecular crosslinking. Thus, repulsive non-covalent electrostatic protein-protein interactions play a dominant role in the formation of multiscale anisotropic structure during SPC extrusion. The formation of an optimal anisotropic SPC extrudate structure is determined by the pH-dependent balance between fibrillar nano-aggregate clustering and electrostatic repulsion. Alkalization or acidification via the water feed implies that protein charge and structure may not be in equilibrium yet with the imposed pH conditions. The transient nature of pH-shifting via the water feed results in an intricate interplay with extrusion conditions. Therefore, control of anisotropic structure formation, via the water feed, in SPC extrudates, is extruder specific.

1. Introduction

In many western countries, a transition from a mostly animal- to a plant-based diet is occurring (Aiking & de Boer, 2020). However, replicating the unique textural properties resulting from the highly hierarchical structural organization of fibers in animal meat is not trivial (Pette & Staron, 1990). Currently, high-moisture extrusion (HME) is the dominant, industrially-scalable, process for creating fibrous texture from plant proteins (Akdogan, 1999) that are commercially available in bulk as isolates, concentrates or flours (Wang et al., 2023). The HME process involves a mixing and hydration step, followed by a thermo-mechanical treatment of the resulting protein dough inside the barrel section of the extruder. The final step involves the cooling of the protein melt, and induces solidification of the protein network. The concomitant contraction of this protein network leads to the

* Corresponding author at: Laboratory of Biophysics, Wageningen University & Research, Stippeneng 4, 6708 WE Wageningen, The Netherlands.
** Corresponding author.
E-mail addresses: john.vanduynhoven@wur.nl (J.P.M. van Duynhoven), camilla.terenzi@wur.nl (C. Terenzi).
[1] These authors contributed equally to this work as co-first authors.

https://doi.org/10.1016/j.foodhyd.2025.111456
Received 17 January 2025; Received in revised form 1 April 2025; Accepted 14 April 2025
Available online 30 April 2025

expulsion of water (Van der Sman & Van der Goot, 2023). When the rates of protein network solidification and contraction are balanced, phase separation into protein- and water-rich domains at a μm scale occurs (Van der Sman & Van der Goot, 2023; Zhang et al., 2022). By shearing the protein melt during cooling, these phase-separated protein-rich domains become elongated along the extrusion direction, and give rise to anisotropic lamellar structures at a larger, sub-mm, scale (Kuijpers et al., 2024; Van der Sman & Van der Goot, 2023). Models describing both phase-separation (Kaunisto et al., 2024) as well as fiber formation (Van der Sman & Van der Goot, 2023; Zhang et al., 2022), mostly lack quantitative experimental verification.

It is generally accepted that transient molecular-level interactions during the thermo-mechanical treatment in the barrel section become fixed *before* the hot protein mass enters the cooling die (Liu & Hsieh, 2008; Van der Sman & Van der Goot, 2023). Within the barrel section, non-covalent bonds become dissociated above the denaturation temperature and exchange between sulfhydryl (SH) and disulfide (SS) groups takes place, which in turn promotes the formation of inter-molecular crosslinks (Osen et al., 2015; Van der Sman & Van der Goot, 2023; Ubbink & Muhialdin, 2022). Under the strongly sheared flow inside the extruder barrel, proteins aggregate and align along the flow direction at the nm scale (Garina et al., 2024; Van der Sman & Van der Goot, 2023; Verbeek & Van den Berg, 2010). The principles of controlling the fibrous structure of extrudates by adjusting HME process conditions have been outlined earlier (Cornet et al., 2021; Van der Sman & Van der Goot, 2023; Wang et al., 2023). Whether such a fibrous structure can eventually be obtained depends largely on the choice of commercially available protein ingredients (Wang et al., 2023). In this respect, protein solubility has been proposed as a parameter that can be used to predict the formation of anisotropic protein structures during HME (Gao et al., 2024; Webb et al., 2023). Protein solubility is considered to be a proxy for protein hydrophobicity and surface charge and is, thus, also closely related to zeta potential (Gao et al., 2024; Grossmann & McClements, 2023). Both protein solubility and zeta potential depend on pH (Grossmann & McClements, 2023; Ma et al., 2022), which offers an opportunity to control protein structure formation during HME. As to the underlying mechanism, a role has been attributed to pH-mediated protein surface charge (Grossmann & McClements, 2023) and to its effect on the electrostatic repulsion between protein molecules. Close to the iso-electric point (pI), the net charge is near zero and minimal electrostatic repulsion is present, which has been shown to promote random aggregation of proteins into particle-like structures. At pH > pI, the electrostatic repulsion between proteins results in fibrillar aggregates (Krebs et al., 2009; van der Linden & Venema, 2007). Besides these charge-mediated mechanisms, SH/SS exchange has been proposed as a pH dependent mechanism for formation of covalent inter-molecular protein crosslinks (Creighton, 1984; Rombouts et al., 2010). Monahan et al. (1995) have shown that, at mild elevated temperatures around 70 – 90 °C, SH/SS interchange occurs for whey protein gels even at pH < 7 (Monahan et al., 1995). In a first systematic study of pH-shifting of plant proteins for use in HME (Muhialdin & Ubbink, 2023), pea protein isolate dispersions were prepared with alkalized or acidified water. Upon resting, these pH-shifted dispersions were pumped into an extruder and a significant effect on hardness and swelling in water was observed. In an alternative approach, pH-shifted dispersions were spray-dried in order to obtain powders that could conventionally be dosed into the feeder of an extruder (Nisov et al., 2022). Also here, a significant effect of pH-shifting on anisotropic structure of extrudates could be observed. Thus, pH-shifting presents an attractive route to control structure and texture of plant-protein extrudates. However, both aforementioned pH-shifting methods are too cumbersome to be implemented on an industrial scale. Ellwanger et al. (2024) showed a more scalable pH-shifting approach by acidifying the extruder water feed (Ellwanger et al., 2024). In contrast to previous approaches, the latter does not necessarily allow for equilibration of protein charge and structure at the applied pH conditions. Results showed that extrudates of soy (Ellwanger et al., 2024) or pea protein isolate (Muhialdin & Ubbink, 2023), become increasingly hard and solid with pH decreasing from neutral conditions down to ~pI. Yet, little variation in protein extractability of pH-shifted extrudates in a reducing solvent was observed, pointing to a limited effect of pH on covalent SS crosslinking (Ellwanger et al., 2024).

In the present work, alkalization and acidification of the extruder water feed was explored as a means to control multiscale anisotropic structure of soy protein concentrate (SPC) extrudates. SPC was chosen due to its industrial potential as an ingredient with high structuring capacity at relatively low cost. Textural functionality of pH-shifted extrudates was determined by hardness measurements with a texture analyzer. Protein extractability in denaturing and reducing solvents was assessed to semi-quantify the effect of pH-shifting on covalent and non-covalent protein crosslinking (Liu & Hsieh, 2008; Verfaillie et al., 2024). To enable the characterization of the multiscale structure of SPC extrudates at complementary and overlapping length scales, multiple measuring modalities were deployed. Small-Angle Neutron or X-ray Scattering (SANS, SAXS) measurements were performed to assess the effect of pH on protein aggregation at the nm-μm scale (Garina et al., 2024), while Magnetic Resonance Imaging (MRI) data, processed using an in house developed method called Rotational Fourier Transform (RFT) (Gobes et al., 2025), enabled quantitative mapping of anisotropic SPC structures at the μm-mm scale (Kuijpers et al., 2024). Diffusive Reflectance (DR) measurements were performed to semi-quantify the effect of pH-shifting on anisotropic structure formation at μm scale (Ranasinghesagara et al., 2006; Van Beers et al., 2017).

2. Materials and methods

2.1. Materials

Commercial SPC (Arcon SJ® IP, 93% DM with 69% protein in dry base, 4% fat, 19% dietary fiber and carbohydrates and 2% ash) from Solae (St. Louis, MO, USA) was used. The acidity and alkalinity of the water feed were adjusted by food-grade citric acid (CA, Merck, Germany) or food-grade trisodiumphosphate (TSP, Merck, Germany), respectively. The molarity of the acidic and alkaline solutions, respectively, ranged from 0 to 0.35 M for CA and from 0 to 0.25 M for TSP. CA and TSP were chosen due to their widespread use as food-grade acid and base.

2.2. Differential scanning calorimetry (DSC) and wide angle X-ray diffraction measurements (WAXD)

DSC measurements on non-hydrated SPCs were performed using a Perkin Elmer DSC8000 instrument. An amount of 30 mg of non-hydrated SPC was weighed on a steel pan, and heated from 5 to 90 °C at 10 °C/min, held at 90 °C for 1 min, and cooled to 5 °C at 10 °C/min, held at 5 °C for 2 min and then heated to 90 °C at 10 °C/min. DSC measurements were also performed on hydrated samples, using a TA DSC Q200 instrument with a protocol adapted from Verfaillie et al. (2023), with 30 mg SPC in the presence of 80% (w/w) moisture (Verfaillie et al., 2023). The hydrated sample was heated to 180 °C at 5 °C/min, cooled down and then reheated to 180 °C at the same heating rate. The endothermic peak observed during the first heating, and absent in the second heating, was used to calculate the denaturation enthalpy per gram of protein.

WAXD measurements were performed on a Bruker D8 Discover X-ray diffractometer in a theta/theta configuration. One dimensional X-ray diffraction patterns were determined from the 2D images using the GADDS (version 1.28) software. The obtained X-ray diffraction patterns were imported in the Bruker EVA software (version 12.0) and relative intensities were determined.

2.3. Protein solubility and zeta potential

Dispersions of 1% w/w and 2.5% w/w SPC were made using demineralized water. The pH of the dispersions was adjusted from 2 up 12 using 1M CA and 0.5M TSP stock solutions. The dispersions were mixed in 50 ml Greiner tubes on a roller bank at room temperature for 16 h. The pH of dispersions was measured, followed by sample centrifugation at 4000 g for 30 min at 20 °C with a swing-out rotor using an acceleration setting of 9. The supernatant was decanted into a new set of 50 ml Greiner tubes and weighed. For the 1% w/w protein dispersions, the total protein content of the supernatant and the dry protein concentrate was determined with Dumas nitrogen combustion method (Elementar Rapid Max *N* Exceed, Germany) using a protein conversion factor of 5.71. Protein solubility was calculated as the percentage of solubilized proteins in the supernatant with regard to total dispersed protein. Measurements were performed in triplicate.

For measuring the zeta potential, a 2.5% w/w SPC dispersion was injected into a disposable folded capillary cell. The capillary cell was placed into a temperature-controlled holder (25 °C) and the electrophoretic mobility was measured by a Zeta Sizer Nano Sizer (ZEN3600, Malvern instruments, UK). Three replicates were measured per sample.

2.4. pH measurements

The pH of extrudates was measured using a pH-meter (Metrohm, 913 pH Meter, Switzerland) equipped with a combined electrode (Metrohm, Spearhead electrode) and temperature sensor (Metrohm, Pt1000 temperature sensor). The pH-shifted SPC extrudates were measured by directly piercing the pH electrode into the extrudate sample. Measurements were performed in duplicate.

2.5. High moisture extrusion

Extrusion trials were performed using a co-rotating twin-screw extruder (XTS 19, Xtrutech, UK) with a screw diameter of 19 mm and length-to-diameter (L/D) ratio of 25. A rectangular cooling die (17 mm (width) × 7 mm (height) × 300 mm (length)) was coupled to the extruder through a die adapter, and a breaker plate was placed before the cooling die.

The extruder barrel was segmented into four temperature-controlled zones, heated to 80 °C, 120 °C, 160 °C, and 135 °C in zones 1 to 4. The die temperature was set at 135 °C. The dry protein concentrate was fed into the extruder with a volumetric feeder (Brabender Technologie, Utrecht, Netherlands). Water was injected via an inlet channel with the use of a constant-flow pump (Master Flex Easy Load II, USA). pH-shifted extrudates were obtained by changing the liquid feed between tap water and different molarities of CA (0.025 M, 0.05 M, 0.075 M, 0.1 M, 0.25 M and 0.35 M) and TSP (0.05 M, 0.075 M, 0.1 and 0.25 M) as described by Ellwanger and co-workers (Ellwanger et al., 2024).

The extrusion trials were run at the screw speed of 350 rpm and moisture content of ca. 60%, keeping a constant throughput of product at 5 kg/h. The cooling water for the cooling die was maintained at a temperature of 65 °C. Once steady-state HME process conditions were reached, the extrudate samples were collected from the cooling die outlet. The samples were placed in a zip-lock bag, immediately cooled in ice-water, frozen and stored at −18 °C. Samples were measured in the thawed state. We note that freeze-thawing may impart structural changes. However, in commercial supply chains, HM extrudates are also stored frozen and this is, thus, taken as a starting condition in this study.

Additionally, pH-shifting using water feed CA molarities of 0.0 M, 0.025 M, 0.05 M and 0.075 M, was performed using a pilot scale PolyTwin extruder (Bühler, Switzerland) to study the effect of extruder scale. This extruder has a screw diameter of 44 mm and an L/D ratio of 34. The cooling die is rectangular with rounded edges (40 mm (width) × 11 mm (height) × 1200 mm (length)) and was maintained at a temperature of 65 °C. The extruder barrel was segmented into four temperature-controlled zones, heated to 30 °C, 140 °C, 180 °C, and 105 °C in zones 1 to 4. The screw speed was maintained at 190 rpm with a moisture content of ca. 60% and a constant product throughput of 57.5 kg/h.

2.6. Hardness measurements

Measurements were performed using a texture analyzer (TA.XT plus, Stable Micro Systems, United Kingdom) equipped with a mini Kramer-cell, consisting of five parallel dull blades. Extrudate ribbons were cut into 2.4 cm pieces using a flat knife, with sample dimensions of 2.4 × 1.8 × 0.7 cm^3 (L × W × H). The blades of the mini Kramer-cell were placed perpendicular to the extrusion direction. The surface was compressed a single time by 4 mm with a speed of 1 mm/s. Data collection started after a trigger force of 0.1 N was reached. Hardness values are presented as the average over measurements on ten extrudate samples of the same ribbon.

2.7. Diffuse reflectance (DR)

Structural anisotropy was assessed via diffuse light reflectance (Ranasinghesagara et al., 2006; Van Beers et al., 2017). The incident light of a linear polarized He-Ne laser (Lumentum model 1108/P, class CDRH II) with a wavelength of 633 nm and a beam diameter of 0.48 mm was applied on extrudate samples at an angle of $\alpha = 70°$. The extrudate samples were placed with the flow direction parallel to the incident laser beam. To prevent ambient light from influencing the measurement, the system was covered by an optical enclosure built from Thorlabs components (Thorlabs, Germany). The spot of diffusely scattered light, with a diameter of around 1 cm, was captured by a Mako G-234C color camera and processed by the Halcon 21.11 software package (MVTec, Germany) using a custom made Halcon script (Imfaimon, Barcelona, Spain) that calculates the major axis length (R_1) and the minor axis length (R_2) of a fitted ellipse. The structural Anisotropy Index as determined by diffuse reflectance (AI(DR)) was calculated as $(R_1/R_2 - 1)$, providing values between 0 (isotropic) and 1 (anisotropic).

2.8. Protein extractability

Samples of approximately 2 cm in length were cut from extrudate ribbon and flash-frozen by keeping a round-bottom flask containing the samples in liquid nitrogen for 30 s. The frozen samples were subsequently freeze-dried over a period of 5 days at −80 °C. Freeze-dried samples were ground to a fine powder. Protein extractability in plain, denaturing and reducing buffers was determined according to an established procedure (Verfaillie et al., 2024).

2.9. Magnetic Resonance Imaging (MRI)

2.9.1. Sample preparation

A frozen extrudate ribbon, of approximately 3 cm in length, was swollen in tap water overnight at 4 °C in a 50 mL tube, using a water:sample weight ratio of 15:1. Swelling substantially increases ^{1}H MRI signal-to-noise ratio and the contrast between protein-rich and water-rich phases, emphasizing the lamellar structure visible by MRI (Kuijpers et al., 2024). After swelling, excess moisture was removed from the outer surface of the extrudate using a paper towel. The sample was placed in a 25 mm NMR tube and sealed with parafilm to prevent water evaporation.

2.9.2. MRI measurements

^{1}H MRI measurements were performed using a 600 MHz (14 T) wide-bore MRI spectrometer (Ascend 600WB Avance NEO, Bruker, Germany) equipped with a 1.5 T/m imaging gradient system (Micro 2.5, Bruker, Germany) and a 25 mm diameter quadrature ^{1}H probe (MicWB40/025 QTR, Bruker, Germany). The duration of the radio frequency (r.f.) 90° excitation and 180° refocusing pulses was optimized to 2.1 ms at 0.4 W and 1.7 ms at 5.3 W, respectively, for all MRI measurements, using ParaVision version 3.3 software.

Extrudates were measured using the Rapid Acquisition with Relaxation Enhancement (RARE) sequence (Hennig et al., 1986). Acquisition parameters were set as follows: echo time, T_E = 10.5 ms; repetition time, T_R = 500 ms; RARE-factor of 3; a total of 8 averages and 8 slices recorded per image acquisition; field-of-view (FOV) of 30 × 12 mm^2, respectively for images in the sagittal plane; in-plane spatial resolution of 39 × 39 × 500 μm^3. The total measurement duration per image acquisition was 7 min.

2.9.3. Analysis of MRI data

^{1}H MRI data processing and image analysis was performed in MATLAB R2022b, using the pvmatlab package from Bruker to extract the data from ParaVision version 3.3. In house scripts for automated data processing were written using either standard MATLAB functions or functions provided by the Image Processing Toolbox version 11.6 and Curve Fitting Toolbox version 3.8 from MATLAB.

The methodology used to calculate the Weighted Order Parameter (WOP) is described elsewhere (Gobes et al., 2025). ImageJ (FIJI, 64-bit) version 1.54j (Schindelin et al., 2012) was used with the RFT plugin version 0.1 installed (Gobes et al., 2025). Images were analyzed using a window size of 25 pixels and 75% overlap between adjacent windows. Angle probability data was further processed using an in house developed routine (Gobes et al., 2025) written in Python 3.12, to convert angle probability into 2D spatial maps of feature angle, relative angle intensity and WOP.

2.10. Slice preparation for small-angle scattering (SAS)

The preparation of sample slices for SAS measurements was performed according to the protocol described elsewhere (Garina et al., 2024). Using a cryo-microtome (Cryostar NX70, Thermo Fisher Scientific, Germany), the samples were sliced at a thickness of 500 μm. The specimen head and blade temperatures used for sectioning were, respectively, −12 °C and −10 °C. To secure the samples to the specimen holder, the materials were embedded into the Tissue-Tek® O.C.T. Compound (Sakura Finetek, USA) embedding medium. To ensure the slice stability during storage at −18 °C, the obtained slices were kept between microscope slides covered with Ultralene thin film (Spex® SamplePrep, USA) and then sealed. Prior to SAS measurements, the slides and Ultralene film were removed.

2.11. Small-angle neutron scattering (SANS)

2.11.1. SANS experimental procedure

SANS measurements were performed on the Larmor Instrument at the ISIS Neutron and Muon Source (STFC Rutherford Appleton Laboratory, UK) (ISIS Larmor, 2023). Using an incidence wavelength range of 0.9 – 13 Å, the time-of-flight configuration at ISIS allowed for simultaneous Q-range of 0.005 – 0.7 Å^{-1}. The parameter Q describes the magnitude of the scattering angle, defined as:

$$Q = \frac{4\pi}{\lambda} \sin\theta, \tag{1}$$

where 2θ represents the scattering angle, and λ stands for the incident neutron wavelength.

Given the anisotropic nature of the samples, the instrument was set up with a symmetric squared sample aperture (6 × 6 mm^2). Extrudate samples were placed into gel cell sample holders with demountable quartz windows to maintain an air-tight environment during the measurements.

2.11.2. SANS data analysis

The SANS data analysis procedure was performed according to the protocol described elsewhere (Garina et al., 2024). Briefly, all two-dimensional (2D) scattering data were processed with the instrument-specific software Mantid (Arnold et al., 2014). By choosing various wavelength bands during data reduction, it was confirmed that no multiple scattering effects were present in the observations. The raw data was placed on an absolute scale (cm^{-1}) corrected for detector sensitivity. The scattering background of the quartz windows was subtracted. For all 2D SANS data, the measured scattering intensities were averaged over a sector, with width of ±15°, for both directions parallel (∥) and perpendicular (⊥) to the alignment direction, as shown in Fig. S3 in SI. The SasView software (Doucet et al., 2022) was used to fit these sector averages. The shape-independent empirical broad peak model was applied to fit the data. The model is given by:

$$I(Q) = \frac{A}{Q^n} + \frac{C}{1 + (|Q - Q_0|\,\xi)^m} + B, \tag{2}$$

where A represents the power-law scale factor, n denotes the power-law exponent, C is the Lorentzian scale factor, ξ is the Lorentzian correlation length, m refers to the exponent of the Lorentz function, B is the flat background that accounts for incoherent scattering from the hydrogenous material. Q_0 is the peak position corresponding to the characteristic center-to-center distance (D) between the scattering inhomogeneities, where $D = 2\pi/Q_0$. The first term A/Q^n becomes a key parameter to evaluate the clustering strength.

Insights into nano-structural anisotropy were obtained through the analysis of the annular intensity averages. The 2D SANS data was averaged over a limited Q-range, $Q_{min} < Q < Q_{trans}$, where Q_{min} represents the lowest measurable scattering vector, and Q_{trans} corresponds to the transition from isotropic to anisotropic structure takes place. The obtained annular intensity averages were fitted with a Legendre series expansion as outlined in Burger et al. (2010):

$$I(Q, \phi) = \sum_{n=0}^{\infty} a_n P_{2n}(\cos\phi^*), \tag{3}$$

where $\phi^* = \phi - (\phi_0) + \frac{\pi}{2}$, with ϕ_0 denoting the orientation angle, a_n are fitting coefficients, and P_{2n} are even Legendre polynomials. From Eq. (3), the nematic order parameter, $\overline{P_2}$, was calculated as:

$$\overline{P_2} = \frac{a_1}{5a_0}. \tag{4}$$

The value of $\overline{P_2}$ indicates the degree of nano-alignment around a certain orientation angle, ϕ_0: the closer $\overline{P_2}$ is to zero, the more isotropic the sample. The maximum value of the order parameter is defined by the scattering characteristics of a perfectly aligned structure.

2.12. (Ultra-)small-angle X-ray scattering ((U)SAXS)

2.12.1. (U)SAXS experimental procedure

SAXS and USAXS measurements were performed on the upgraded beamline ID02 of the European Synchrotron Radiation Facility (ESRF, Grenoble, France) (Narayanan et al., 2022). A long evacuated detector tube facilitated an automated change of the sample-to-detector distance (SDD) from 1 to 30.9 m, allowing for the SAXS and USAXS data collection using the same setup. Three SDDs (1, 8, and 30.9 m) were employed to cover a Q range of 0.0002 – 0.8 Å^{-1} with an X-ray wavelength of 1.014 Å.

Sample slices were positioned on the sample holder. The holder was covered with an Ultralene film, which was sealed with double-sided tape. This was intended to ensure an air-tight environment. The small beam size of 100 × 150 μm^2 (vertical × horizontal) allowed for probing 20 measurement frames over a length of 8 mm in the plane perpendicular to the extrusion direction.

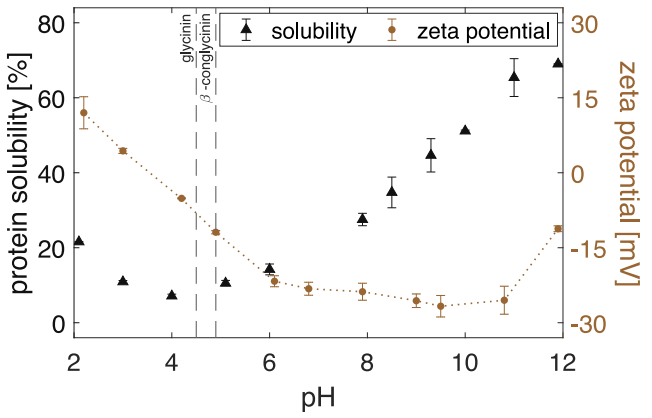

Fig. 1. Protein solubility (black solid triangles) and zeta potential (gray solid circles) data for SPC dispersions as a function of pH. Error bars refer to duplicate measurements. Vertical lines indicate pI values for soy proteins from literature (Koshiyama, 1968, 1972; Myśliwiec et al., 2016).

2.12.2. (U)SAXS data analysis

All 2D scattering data was reduced and normalized to an absolute scale (cm^{-1}) following standard procedures (Narayanan et al., 2022). The instrument-specific software SAXSutilities (Sztucki, 2021) was utilized for scattering background subtraction of the Ultralene film, merging measurements recorded at different SDDs and other specific operations. Averaging was performed according to the protocol described elsewhere (Garina et al., 2024) to account for material heterogeneity. It was investigated whether the merged intensity curves exhibited characteristic shoulder-like features or obeyed a power-law at some Q regions.

3. Results and discussion

3.1. Characterization of SPC

Protein characteristics, such as level of denaturation and solubility, can vary significantly among different commercially available protein sources. Hence, we characterized composition and structural features of the Arcon® SJ SPC that was used as ingredient for manufacturing extrudates. No denaturation enthalpy was detected by DSC measurements at 80% moisture. When this material was measured as is, a denaturation enthalpy of 2.9 J/gram protein was observed, which points to the presence of residual secondary structure. This finding was confirmed by WAXD measurements, which showed diffraction lines at 4.6 Å corresponding to the presence of β-sheet structures (Clark & Lee-Tuffnell, 1986; Yuryev et al., 1990). The assignment of the denaturation enthalpy measured in non-hydrated state to residual β-sheet structure is corroborated by the observed correlation between DSC and WAXD for a range of protein concentrates and isolates shown in SI Fig. S5.

Results of solubility and zeta potential measurements for Arcon® SJ SPC are shown in Fig. 1. At pH 4, the solubility is low and the zeta potential is about zero, which is lower than the reported pI values for soy proteins, respectively 4.6 and 4.9 for glycinin and β-conglycinin Koshiyama (1968, 1972). We attribute this to the presence of cell-wall polysaccharides, such as cellulose and pectin, that generally have pI < 3 (Myśliwiec et al., 2016). At pH > pI the zeta potential decreases, thus the net negative surface charge and solubility increase. At pH 7, the zeta potential reaches a plateau, while the solubility continues to increase. This is likely due to partial protein unfolding at increasingly more alkaline pH conditions (Lagrain et al., 2010).

3.2. Effect of pH on multiscale anisotropic structure formation

3.2.1. Hardness and structural anisotropy

Fig. 2A–B shows the results of structural anisotropy measured by AI(DR) (red solid triangles) and of extrudate hardness measurements (blue solid circles). Near the pI ~ 4.2, hardness and AI(DR) are both roughly a factor 3 lower than their respective highest value near neutral pH. At pH ~ pI, a weak network is formed that lacks an anisotropic fibrous structure at the μm scale. This lack of structure can be attributed to the absence of charges electrostatically shielding the proteins (Fig. 1), which in turn promotes particulate protein aggregation and yields the formation of a weak isotropic network (Chen et al., 2017; van der Linden & Venema, 2007; Muhialdin & Ubbink, 2023). At pH > pI, both hardness and AI(DR) values increase towards their optimum value, respectively at pH ~ 6.5 and pH ~ 5.4, which likely corresponds to protein aggregation transitioning from particulate to fibrillar (Krebs et al., 2009; van der Linden & Venema, 2007). At pH >> pI, both the hardness and AI(DR) values decrease, indicating a weakening of the protein network.

The optimum in anisotropic structure formation found for hardness and AI(DR) is in line with the sub-mm scale lamellar phase separation seen in sagittal MRI images of pH-shifted SPC samples, shown in Fig. 2C. At pH ~ pI, the desired lamellar phase-separated structure is nearly absent. At pH ~ 5.4, corresponding to the optimum value observed by AI(DR) measurements, a lamellar phase-separated structure becomes visible and further develops at pH ~ 6.5, where the highest hardness value is observed. Further increasing the pH, away from pI, leads to a loss in the lamellar phase-separated structure. Quantitative analysis of the sagittal MRI images in Fig. 2C using RFT analysis (Gobes et al., 2025) (Fig. S1 in SI) shows that the WOP values, calculated at each pH condition as the spatial average within the corresponding MRI image, follow a non-monotonic pH-dependence (Fig. 2D), and is in good agreement with the behavior found for both the hardness and AI(DR) parameters (Fig. 2A–B).

The non-monotonic pH-dependence found for hardness, AI(DR) and WOP(MRI) parameters show that, at pH ~ pI or pH >> pI, the network structure is weaker compared to that around pH 5.4 – 6.5, at both sub-mm and sub-μm scales. To investigate the role of covalent and non-covalent crosslinking, protein extractability of pH-shifted extrudates has been assessed using non-reducing and reducing denaturing buffers (Liu & Hsieh, 2007; Verfaillie et al., 2024). Protein extractability in a non-reducing denaturing buffer (Fig. S2 in SI) was (39 ± 5)% over the examined pH range and, within the experimental error, it remained unaffected by pH-shifting. This finding suggested a negligible effect of pH on non-covalent crosslinking of proteins. In a reducing denaturing buffer roughly 2.5 times more protein could be extracted, but also this amount remained unaffected by pH-shifting. Therefore we conclude that the amount of *both* covalently and non-covalently crosslinked proteins is unaffected by pH-shifting. This result is in agreement with previous findings from pH-shifting via the extruder water feed of soy protein isolates (Ellwanger et al., 2024).

3.2.2. Sub-μm scale structural order

SANS measurements of pH-shifted SPC extrudates were performed to investigate the anisotropic structure formation at nm to sub-μm length scale. The analysis of such series of SANS data, described in Section 2.11.2, resulted in four independent fitting parameters as a function of pH, namely (i) the correlation length, (ii) the center-to-center distance, (iii) the clustering strength, and (iv) the nematic order parameter. The parameters (i)-(iii) could be separately fitted for the sector averages taken in the directions parallel (∥) or perpendicular (⊥) to the extrusion flow direction (examples of the fit are shown in Fig. S3 (right) in SI).

The correlation length, defined as the size of the smallest discernible scattering object (Tian et al., 2020), has values around 8 – 10 nm for SPC extrudates (Guan et al., 2024). As shown in Fig. 3 (top), at pH

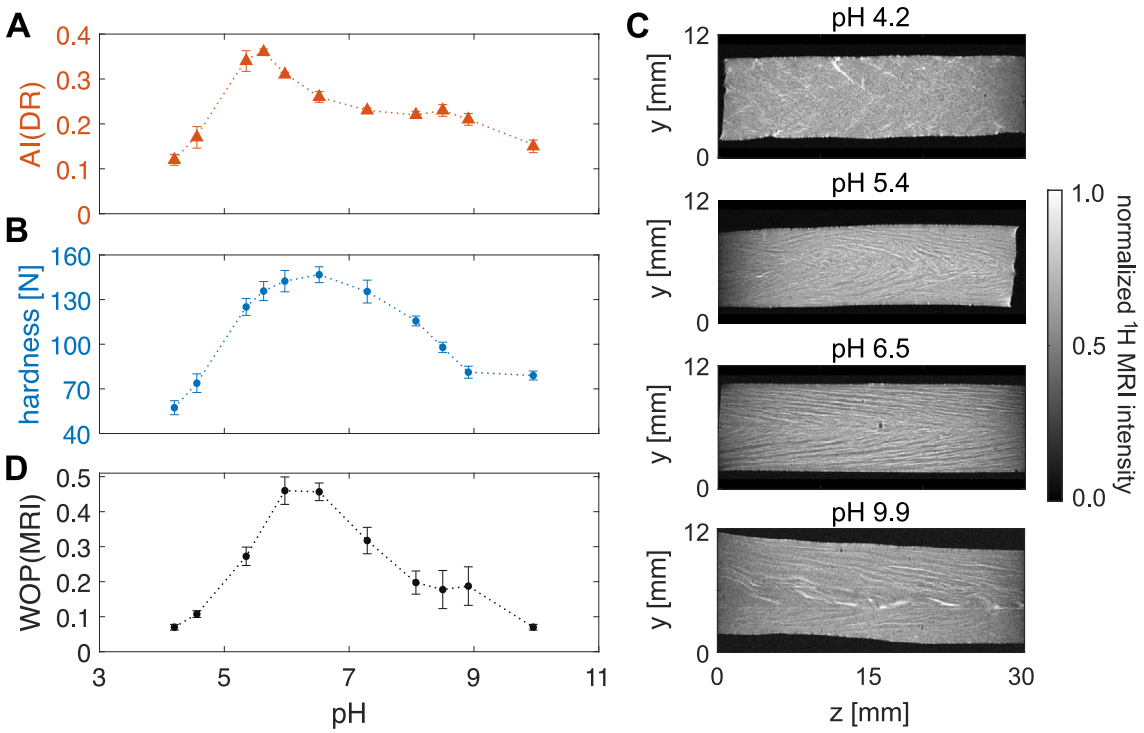

Fig. 2. For pH-shifted SPC extrudates: (A) AI(DR) values (solid orange triangles); (B) Kramer-cell hardness results (blue solid circles); (D) WOP(MRI) values obtained from vector fields maps (Fig. S1 in SI) for sagittal ^{1}H MRI images, in turn displayed for four pH-shifted samples in (C). SI Fig. S4 shows a folded extrudate sample at neutral and acidic pH, respectively illustrating the presence or absence of macroscopic fibrous structure.

7.3 the correlation length was ca. 8 nm, which is close to the diameter values for native glycinin and β-conglycinin molecules (Badley et al., 1975). Upon pH-shifting, the correlation length followed the trend observed for zeta potential and solubility (Fig. 1), first decreasing at acidic conditions and then reaching a plateau at alkaline pH values (Fig. 3 (top)). The correlation length, thus, likely describes (partially) folded globular proteins that, due to a net surface charge, have an 'effective' volume.

The center-to-center distance represents the main distance between scattering objects. Center-to-center distance values of ~35 – 41 nm are generally found for SPC extrudates (Garina et al., 2024; Guan et al., 2024), which is close to the value of ca. 31 nm observed for the SPC extrudate at pH 7.3 (Fig. 3 (bottom)). Similar to the correlation length, the center-to-center distance increases with increasing pH (Fig. 3 (bottom)). We interpret the center-to-center distance to be the size of nano-aggregates consisting of multiple partially folded globular proteins with a characteristic correlation length. The observed increase in correlation length and electrostatic repulsion, due to a higher pH-induced negative net charge on the protein (Fig. 1), yields larger nano-aggregates. Subsequently, these nano-aggregates are clustered together and form a fibrillar network at the sub-μm scale (Garina et al., 2024; Guan et al., 2024). The SANS results provide an explanation for the structural changes shown in Fig. 2 between pH 4 and 7, but cannot account for the decrease in structural order seen at alkaline conditions. One possible explanation is that pH-shifting is accompanied by a change in ionic strength of the liquid phase, which does not affect the structure formation at nm scale and, thus, is not detected by SANS measurements. However, pH-shifting with HCl and NaOH, which have smaller ionic strength contributions, gave similar results as with citric acid and TSP (data not shown).

The clustering strength, A/Q^n, is calculated from the broad-peak model, using $Q = 0.02$ Å^{-1}, since at $Q <$ ca. 0.02 Å^{-1} (corresponding to real-space distances > 60 nm) the power-law behavior becomes dominating. The clustering strength is generally interpreted as a measure of the interaction strength between scattering objects (Hammouda et al., 2004). High and low values of the clustering strength, respectively, are attributed to the presence or absence of network formation (Bayrak et al., 2023; Wu et al., 2018).

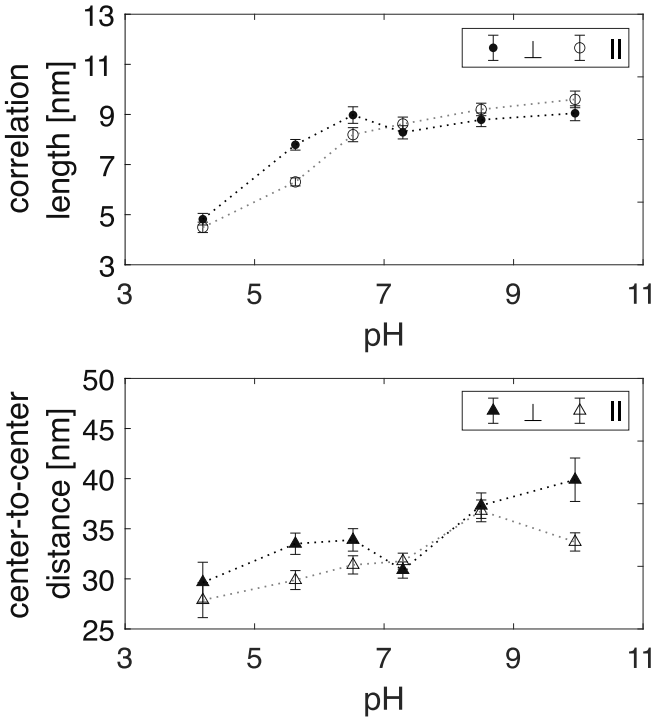

Fig. 3. Correlation length (top) and center-to-center distance values (bottom) estimated from fitting the broad peak model (Eq. (2)) to the SANS sector averages taken in the parallel (∥) or perpendicular (⊥) direction with respect to the extrusion flow direction.

Clustering strength data for pH-shifted SPC extrudates, determined along both directions, are shown in Fig. 4 and follow a similar non-monotonic trend to the AI(DR) and hardness values reported in Fig. 2. This is especially evident for the direction perpendicular to extrusion. Since the clustering strength is determined at the length scales above the size of single nano-aggregates, we interpret it to be a measure of the fibrillar aggregation of these nano-aggregates. At acidic conditions, the clustering strength values measured in both the ∥ and ⊥ direction, as well as the electrostatic repulsion between proteins, (Fig. 1) are low. The latter result was expected for nano-aggregates of these proteins, yielding efficient formation of a network of particulate clusters, rather than of fibril bundles (van der Linden & Venema, 2007), at these pH conditions. The opposite effect is likely seen at alkaline conditions where, due to excessive electrostatic repulsion among nano-aggregates, thin linear chains are formed that do not create a cohesive network (van der Linden & Venema, 2007). At alkaline pH values, the clustering strength is similar for both the ∥ and ⊥ direction and is lower than that at optimum pH, here around pH 7. These results indicate that, when the electrostatic shielding and electrostatic repulsion are balanced, the interaction strength between nano-aggregates is high. This suggests the formation of a cohesive network at optimum pH, and is in agreement with evidence provided by hardness and AI(DR) measurements (Fig. 2).

The nematic order parameter, obtained from SANS data, is a measure of nano-alignment at the length scales of ca. 13 – 125 nm (Tian et al., 2020), and has been shown previously to vary with process conditions during extrusion of SPC (Garina et al., 2024). Results shown in Fig. 4 are in good agreement with the clustering strength data, and provide additional insight in the type of aggregate that these nano-aggregates form. At the optimal pH, the nematic order parameter is higher than at acidic or alkaline conditions, suggesting the presence of fibril alignment along the extrusion direction, and is in line with AI(DR) results Fig. 2. While no fibrillar structure is expected to be present at low pH, aggregates are predominantly fibrillar at high pH. In the latter condition, the observed lower fibril alignment is likely a result of strong electrostatic repulsion among protein molecules in the presence of excessive surface charges (van der Linden & Venema, 2007; Muhialdin & Ubbink, 2023). To further underpin this, Fig. 5 shows (U)SAXS data of these extrudates and qualitatively reveals that, at acidic conditions, indeed a change in aggregation behavior is present. The solid arrow in Fig. 5 points to a low-Q USAXS intensity shoulder region that is associated with fibril formation at the 100 – 200 nm length scale for SPC extrudates (Zink et al., 2024). In Fig. 5, this shoulder is roughly at the same location for neutral and alkaline pH conditions, but it disappears at pH < 6. Thus, at pH ~ pI, fibril formation is hampered and particulate clusters of nano-aggregates, devoid of a well-defined orientation, are formed as also suggested by nematic order parameter and AI(DR) results (Fig. 4). At alkaline conditions, this shoulder is present, confirming that fibrillar aggregates are formed (Krebs et al., 2009; van der Linden & Venema, 2007). These fibrillar aggregates show little interaction, due to excessive electrostatic charges between proteins (Fig. 3), and do not form a cohesive network, in agreement with clustering strength (Fig. 4), AI(DR) and hardness results (Fig. 2). Additionally, a shifting high-Q shoulder is seen in the SAXS data (indicated with the dashed arrow in Fig. 5), which is also visible in the SANS data (Fig. S3 (right) in SI) and used to fit the center-to-center distance. The presence or absence of fibrillar network formation at the nm-μm scale influences protein network contraction during cooling. This respectively results in the formation of lamellar or isotropic phase separation at the mm scale as visible in MRI images in Fig. 2C.

3.3. Interplay of extrusion conditions and pH-shifting

In this work, we shifted the pH of the SPC dough in a lab-scale high-moisture extruder by adjusting the acidic and alkaline molarity of the water feed. In contrast to pH-shifting approaches that involved resting

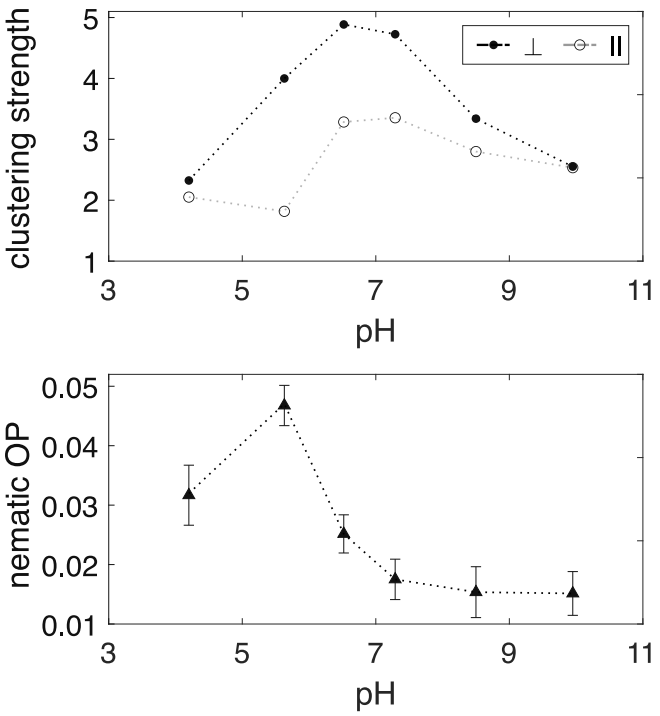

Fig. 4. For pH-shifted SPC extrudates: (top) SANS clustering strength, measured along both directions parallel (∥) and perpendicular (⊥) to extrusion, and (bottom) nematic order parameter, in turn indicative of nano-anisotropy at length scales of ca. 13 – 125 nm. The clustering strength is obtained by fitting the broad-peak model (Section 2.11.2) to the SANS data.

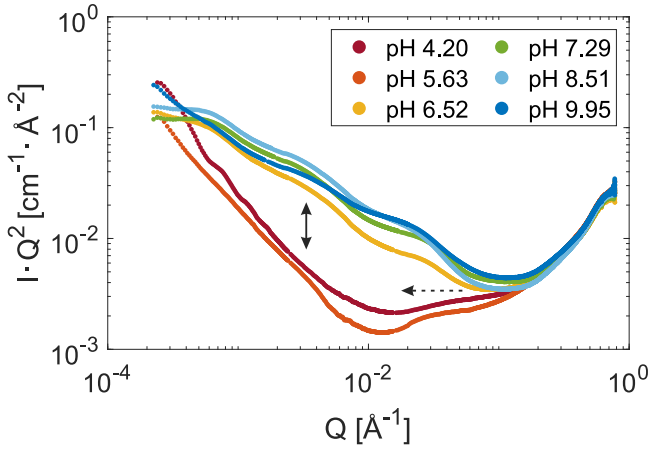

Fig. 5. (U)SAXS results of pH-shifted SPC extrudates. Arrows indicate either a peak shift in the high-Q region for low-pH samples (dashed line) or the disappearance of a low-Q intensity shoulder at low pH (solid line).

of the protein dough (Muhialdin & Ubbink, 2023; Nisov et al., 2022), in our conditions we cannot assume an equilibration of the protein structure and aggregation state. The effect of pH-shifting on AI(DR) for both the lab-scale extruder used in this work, and a pilot-plant-scale extruder, is shown in Fig. 6. In both cases, SPC has been extruded using identical dosed water contents, comparable barrel temperature profiles, as well as screw speeds and throughputs typical for these extruders. For the pilot-plant-scale extruder (green solid triangles) the pH dependence of AI(DR) values is shifted towards higher pH values. This difference between the two extruders is likely due to corresponding differences in equilibration kinetics of protein structure and of non-covalent aggregation at acidic conditions. The pilot-plant extruder has a more extensive mixing section, and specific mechanical energies (SME)

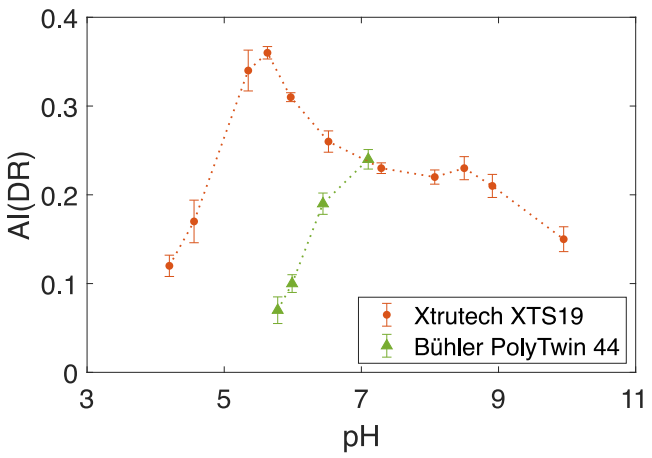

Fig. 6. AI(DR) results for pH-shifted Arcon SJ SPC extrudates using two different scale extruders: a lab-scale Xtrutech XTS19 (orange solid circles), operating at 5 kg/h (blue), and a pilot scale Bühler PolyTwin 44 (green solid triangles), operating at 57.5 kg/h.

are much higher than for those in the lab-scale extruder (Table S1 in SI). Upon acidification of the water feed, this will promote particulate aggregation and, thus, impede anisotropic structure formation. In the lab-scale extruder there is less mixing and SMEs are lower. Hence, upon acidification fibrillar structure formation can still occur. The results in Fig. 6 indicate that anisotropic structure formation is determined by a complex interplay between pH-shifting and extrusion conditions. This finding implies that control of anisotropic structure formation by pH-shifting via the water feed is extruder specific.

4. Conclusions

In this work, we resolved the multiscale structural changes that underlie the observed non-monotonic effect of pH-shifting via the water feed on the hardness of high-moisture extrudates of SPC. A schematic overview of the effects of pH-shifting on multiscale anisotropic extrudate structure is given in Fig. 7. pH-shifting had a non-monotonic effect on the sub-mm anisotropic structure as seen by MRI. Upon pH-shifting towards pH ~ pI, as well as at pH >> pI, MRI images showed an increase in structural disorder and the absence of an anisotropic structure (Fig. 7 top diagrams). This non-monotonic behavior is also observed at the μm scale by AI(DR). SANS data was used to underpin this non-monotonic behavior at the nm scale and showed that, at pH > pI, the correlation length of partially folded globular proteins (Fig. 7 CL) and the size of their nano-aggregates (Fig. 7 CC) monotonically increase with pH. Additionally, SAXS data indicated the concomitant transition from particulate to fibrillar aggregation. The sub-μm scale effect of pH-shifting on the clustering strength and the nematic order parameter of the fibrillar aggregates is, again, non-monotonic (Fig. 7, green dashed arrows). The increase in clustering strength and nematic order at pH > pI is in line with a transition towards fibrillar aggregation. The decrease of clustering strength and nematic order parameter, when pH is further shifted to alkaline conditions, can be explained by electrostatic intra- and inter-fibrillar repulsion (Fig. 7 CS). Protein extractability measurements indicated that the effects of pH-shifting on anisotropic structure formation could not be attributed to covalent intermolecular crosslinking. An optimal anisotropic structure can, thus, be achieved, when a pH-dependent balance between electrostatic repulsion and fibrillar nano-aggregate clustering is struck. This optimum condition, however, is extruder dependent. pH-shifting via the water feed is therefore an industrially-scalable, yet extruder condition specific, technology capable of controlling multiscale anisotropic structure formation of plant proteins.

CRediT authorship contribution statement

Sam A. Kuijpers: Writing – original draft, Visualization, Software, Methodology, Investigation, Formal analysis, Data curation, Conceptualization. **Ekaterina D. Garina:** Writing – review & editing, Visualization, Methodology, Investigation, Formal analysis, Data curation, Conceptualization. **Martijn I. Gobes:** Software, Data curation. **Ruud den Adel:** Methodology, Investigation. **Gregory N. Smith:** Data curation, Formal analysis, Software, Writing – review & editing. **Michael Sztucki:** Data curation, Formal analysis, Software, Writing – review & editing. **Johannes Hohlbein:** Writing – review & editing. **Wim G. Bouwman:** Writing – review & editing, Supervision, Funding acquisition. **John P.M. van Duynhoven:** Writing – review & editing, Supervision, Resources, Funding acquisition, Conceptualization. **Camilla Terenzi:** Writing – review & editing, Supervision, Project administration, Funding acquisition.

Declaration of competing interest

The authors declare the following financial interests/personal relationships which may be considered as potential competing interests: John P.M. van Duynhoven and Ruud den Adel are employed by a company that manufactures and markets plant-based meat alternatives. The other authors declare that they have no known competing financial interests or personal relationships that could have appeared to influence the work reported in this paper.

Acknowledgments

This work is part of the project “Measurement and Modelling of Multiscale Processed Protein Products (MP3)” (with project number 18744) of the research programme OTP TTW, which is financed by the Dutch Research Council, Netherlands as well as by contributions from consortium partners Unilever, Cargill, dsm-firmenich, FrieslandCampina and Wageningen Food and Biobased Research. This project was also supported by the uNMR-NL Grid: A distributed, state-of-the-art Magnetic Resonance facility for the Netherlands (NWO grant 184.035.002). We gratefully acknowledge the Science and Technology Facilities Council (STFC) for access to neutron beamtime at ISIS through RB 2269101 (data are available at https://doi.org/10.5286/ISIS.E.RB2269101). We also acknowledge the European Synchrotron Radiation Facility (ESRF) for the provision of synchrotron radiation facilities (data are available at https://doi.org/10.5281/zenodo.14002334). This work benefited from the use of the SasView application, originally developed under NSF Award DMR-0520547. SasView also contains code developed with funding from the EU Horizon 2020 programme under the SINE2020 project Grant No 654000. We thank Arno Wouters and Kristof Brijs (KU Leuven) for skillfully performing the protein extraction analyses. Finally, we thank Kalyan Panda and Claudia Zimmermann for performing extrusion trials and Gert-Jan Goudappel (Unilever Global Food Innovation Centre, Wageningen) for performing MRI measurements on extrudates.

Appendix A. Supplementary data

Supplementary material related to this article can be found online at https://doi.org/10.1016/j.foodhyd.2025.111456.

Data availability

SANS data are available at https://doi.org/10.5286/ISIS.E.RB2269101. (U)SAXS data are available at https://doi.org/10.5281/zenodo.14002334.

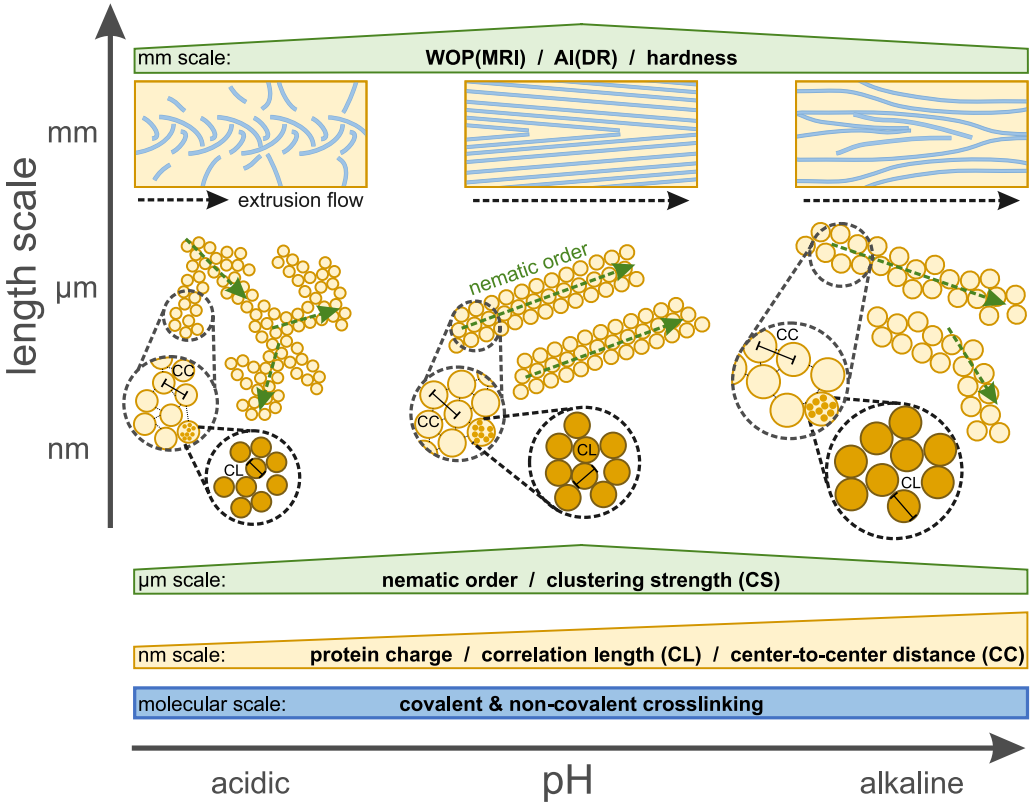

Fig. 7. Schematic summary of the effect of pH-shifting on SPC extrudate structure. These effects are probed at the mm scale, by WOP(MRI), AI(DR) and hardness (Fig. 2) measurements; at the μm scale, by nematic order parameter and clustering strength (Fig. 4); at the nm scale, by correlation length and center-to-center distance (Fig. 3); at the molecular scale by protein extractability.

References

Aiking, H., & de Boer, J. (2020). The next protein transition. *Trends in Food Science & Technology*, *105*, 515–522. http://dx.doi.org/10.1016/j.tifs.2018.07.008.

Akdogan, H. (1999). High moisture food extrusion. *International Journal of Food Science & Technology*, *34*(3), 195–207. http://dx.doi.org/10.1046/j.1365-2621.1999.00256.x.

Arnold, O., Bilheux, J. C., Borreguero, J. M., Buts, A., Campbell, S. I., Chapon, L., Doucet, M., Draper, N., Ferraz Leal, R., Gigg, M. A., Lynch, V. E., Markvardsen, A., Mikkelson, D. J., Mikkelson, R. L., Miller, R., Palmen, K., Parker, P., Passos, G., Perring, T. G., ... Zikovsky, J. (2014). Mantid - Data analysis and visualization package for neutron scattering and μ SR experiments. *Nuclear Instruments and Methods in Physics Research, Section A: Accelerators, Spectrometers, Detectors and Associated Equipment*, *764*, 156–166. http://dx.doi.org/10.1016/j.nima.2014.07.029.

Badley, R. A., Atkinson, D., Hauser, H., Oldani, D., Green, J. P., & Stubbs, J. M. (1975). The structure, physical and chemical properties of the soy bean protein glycinin. *Biochimica Et Biophysica Acta (BBA) - Protein Structure*, *412*(2), 214–228. http://dx.doi.org/10.1016/0005-2795(75)90036-7.

Bayrak, M., Whitten, A. E., Mata, J. P., Conn, C. E., Floury, J., & Logan, A. (2023). Real-time monitoring of casein gel microstructure during simulated gastric digestion monitored by small-angle neutron scattering. *Food Hydrocolloids*, *144*, Article 108919. http://dx.doi.org/10.1016/j.foodhyd.2023.108919.

Burger, C., Hsiao, B. S., & Chu, B. (2010). Preferred orientation in polymer fiber scattering. *Polymer Reviews*, *50*(1), 91–111. http://dx.doi.org/10.1080/15583720903503494.

Chen, N., Zhao, M., Niepceron, F., Nicolai, T., & Chassenieux, C. (2017). The effect of the pH on thermal aggregation and gelation of soy proteins. *Food Hydrocolloids*, *66*, 27–36. http://dx.doi.org/10.1016/j.foodhyd.2016.12.006.

Clark, A. H., & Lee-Tuffnell, C. (1986). Gelation of globular proteins. In J. Mitchell, & D. A. Ledward (Eds.), *Functional properties of food macromolecules* (pp. p203–272). London: Elsevier.

Cornet, S. H., Snel, S. J., Lesschen, J., van der Goot, A. J., & van der Sman, R. G. (2021). Enhancing the water holding capacity of model meat analogues through marinade composition. *Journal of Food Engineering*, *290*, Article 110283. http://dx.doi.org/10.1016/j.jfoodeng.2020.110283.

Creighton, T. E. (1984). Disulfide bond formation in proteins. *Methods in Enzymology*, *107*, 305–329. http://dx.doi.org/10.1016/0076-6879(84)07021-X.

Doucet, M., Cho, J. H., Alina, G., Attala, Z., Bakker, J., Bouwman, W., Bourne, R., Butler, P., Cadwallader-Jones, I., Campbell, K., Cooper-Benun, T., Durniak, C., Forster, L., Gilbert, P., Gonzalez, M., Heenan, R., Jackson, A., King, S., Kienzle, P., ... Wolf, C. (2022). SasView version 5.0.5. http://dx.doi.org/10.5281/zenodo.6331344.

Ellwanger, F., Fuhrmann, M., & Karbstein, H. P. (2024). Influence of lowering the pH value on the generation of fibrous structures of protein gels with different network types. *Gels*, *10*(173), 1–14.

Gao, K., Rao, J., & Chen, B. (2024). Plant protein solubility: A challenge or insurmountable obstacle. *Advances in Colloid and Interface Science*, *324*, Article 103074. http://dx.doi.org/10.1016/j.cis.2023.103074.

Garina, E. D., Adel, R. D., Duynhoven, J. P. M. V., Smith, G. N., Dalgliesh, R. M., Sztucki, M., & Bouwman, W. G. (2024). SANS and SAXS : A Love Story to unravel structural evolution of soy proteins and polysaccharide fibres during high moisture extrusion for meat alternatives. *Food Hydrocolloids*, *155*, Article 110121. http://dx.doi.org/10.1016/j.foodhyd.2024.110121.

Gobes, M. I., Kuijpers, S. A., Terenzi, C., Van der Sman, R., Van Duynhoven, J. P. M., & Hohlbein, J. (2025). Rotated Fourier transform (RFT) enables the quantification of anisotropic structure in high moisture plant-protein extrudates. (Under review in Food Structure).

Grossmann, L., & McClements, D. J. (2023). Current insights into protein solubility: A review of its importance for alternative proteins. *Food Hydrocolloids*, *137*, Article 108416. http://dx.doi.org/10.1016/j.foodhyd.2022.108416.

Guan, T., Sägesser, C., Villiger, R., Zychowski, L., Kohlbrecher, J., Dumpler, J., Mathys, A., Rühs, P., Fischer, P., & Matsarskaia, O. (2024). In situ studies of plant-based meat analog texturization. *Food Hydrocolloids*, *155*, http://dx.doi.org/10.1016/j.foodhyd.2024.110215.

Hammouda, B., Ho, D. L., & Kline, S. (2004). Insight into clustering in poly(ethylene oxide) solutions. *Macromolecules*, *37*(18), 6932–6937. http://dx.doi.org/10.1021/ma049623d.

Hennig, J., Nauerth, A., & Friedburg, H. (1986). RARE imaging: A fast imaging method for clinical MR. *Magnetic Resonance in Medicine*, *3*(6), 823–833. http://dx.doi.org/10.1002/mrm.1910030602.

ISIS Larmor 2023. https://www.isis.stfc.ac.uk/Pages/Larmor.aspx. [Accessed 21 July 2023].

Kaunisto, E., Wassén, S., & Stading, M. (2024). A thermodynamical finite element model of the fibre formation process during extrusion of high-moisture meat analogues. *Journal of Food Engineering*, *362*, http://dx.doi.org/10.1016/j.jfoodeng.2023.111760.

Koshiyama, I. (1968). Chromatographic and Sedimentation Behavior of a Purified 7S Protein in Soybean Globulins. *Cereal Chemistry*, *45*, 405–412.

Koshiyama, I. (1972). Purification and physico-chemical properties of 11s globulin in soybean seeds. *International Journal of Peptide Protein Research*, (4), 167–176.

Krebs, M. R., Domike, K. R., & Donald, A. M. (2009). Protein aggregation: More than just fibrils. *Biochemical Society Transactions*, *37*(4), 682–686. http://dx.doi.org/10.1042/BST0370682.

Kuijpers, S. A., Goudappel, G.-J., Huppertz, T., Van Duynhoven, J. P., & Terenzi, C. (2024). Quantification of phase separation in high moisture soy protein extrudates by NMR and MRI. *Food Research International*, *197*, Article 115225. http://dx.doi.org/10.1016/j.foodres.2024.115225.

Lagrain, B., Vleeschouwer, K. D., Rombouts, I., Brijs, K., Hendrickx, M. E., & Delcour, J. A. (2010). The kinetics of β-elimination of cystine and the formation of lanthionine in gliadin. *Journal of Agricultural and Food Chemistry*, *58*(19), 10761–10767. http://dx.doi.org/10.1021/jf102575r.

van der Linden, E., & Venema, P. (2007). Chapter 4. Similarities in self-assembly of proteins and surfactants: An attempt to bridge the gap. *Food Colloids*, 57–67. http://dx.doi.org/10.1039/9781847557698-00057.

Liu, K. S., & Hsieh, F. H. (2007). Protein-protein interactions in high moisture-extruded meat analogs and heat-induced soy protein gels. *JAOCS, Journal of the American Oil Chemists' Society*, *84*(8), 741–748. http://dx.doi.org/10.1007/s11746-007-1095-8.

Liu, K. S., & Hsieh, F. H. (2008). Protein-protein interactions during high-moisture extrusion for fibrous meat analogues and comparison of protein solubility methods using different solvent systems. *Journal of Agricultural and Food Chemistry*, *56*(8), 2681–2687. http://dx.doi.org/10.1021/jf073343q.

Ma, K. K., Greis, M., Lu, J., Nolden, A. A., McClements, D. J., & Kinchla, A. J. (2022). Functional performance of plant proteins. *Foods*, *11*(4), 1–23. http://dx.doi.org/10.3390/foods11040594.

Monahan, F. J., German, J. B., & Kinsella, J. E. (1995). Effect of pH and temperature on protein unfolding and thiol/ disulfide interchange reactions during heat-induced gelation of whey proteins. *Journal of Agricultural and Food Chemistry*, *43*(1), 46–52. http://dx.doi.org/10.1021/jf00049a010.

Muhialdin, B. J., & Ubbink, J. (2023). Effects of pH and aging on the texture and physicochemical properties of extruded pea protein isolate. *Food Hydrocolloids*, *140*, Article 108639. http://dx.doi.org/10.1016/j.foodhyd.2023.108639.

Myśliwiec, D., Chylińska, M., Szymańska-Chargot, M., Chibowski, S., & Zdunek, A. (2016). Revision of adsorption models of xyloglucan on microcrystalline cellulose. *Cellulose*, *23*(5), 2819–2829. http://dx.doi.org/10.1007/s10570-016-0995-x.

Narayanan, T., Sztucki, M., Zinn, T., Kieffer, J., Homs-Puron, A., Gorini, J., Van Vaerenbergh, P., & Boesecke, P. (2022). Performance of the time-resolved ultra-small-angle X-ray scattering beamline with the Extremely Brilliant Source. *Journal of Applied Crystallography*, *55*(1), 98–111. http://dx.doi.org/10.1107/S1600576721012693.

Nisov, A., Nikinmaa, M., Nordlund, E., & Sozer, N. (2022). Effect of pH and temperature on fibrous structure formation of plant proteins during high-moisture extrusion processing. *Food Research International*, *156*, Article 111089. http://dx.doi.org/10.1016/j.foodres.2022.111089.

Osen, R., Toelstede, S., Eisner, P., & Schweiggert-Weisz, U. (2015). Effect of high moisture extrusion cooking on protein–protein interactions of pea (Pisum sativum L.) protein isolates. *International Journal of Food Science & Technology*, *50*(6), 1390–1396. http://dx.doi.org/10.1111/ijfs.12783.

Pette, D., & Staron, R. S. (1990). Cellular and molecular diversities of mammalian skeletal muscle fibers. *Reviews of Physiology, Biochemistry and Pharmacology*, *116*, 1–76. http://dx.doi.org/10.1007/3540528806_3.

Ranasinghesagara, J., Hsieh, F., & Yao, G. (2006). A photon migration method for characterizing fiber formation in meat analogs. *Journal of Food Science*, *71*(5), E227–E231. http://dx.doi.org/10.1111/j.1750-3841.2006.00038.x.

Rombouts, I., Lagrain, B., Brijs, K., & Delcour, J. A. (2010). β-Elimination reactions and formation of covalent cross-links in gliadin during heating at alkaline pH. *Journal of Cereal Science*, *52*(3), 362–367. http://dx.doi.org/10.1016/j.jcs.2010.06.006.

Schindelin, J., Arganda-Carreras, I., Frise, E., Kaynig, V., Longair, M., Pietzsch, T., Preibisch, S., Rueden, C., Saalfeld, S., Schmid, B., Tinevez, J. Y., White, D. J., Hartenstein, V., Eliceiri, K., Tomancak, P., & Cardona, A. (2012). Fiji: An open-source platform for biological-image analysis. *Nature Methods*, *9*(7), 676–682. http://dx.doi.org/10.1038/nmeth.2019.

Van der Sman, R. G., & Van der Goot, A. J. (2023). Hypotheses concerning structuring of extruded meat analogs. *Current Research in Food Science*, *6*, Article 100510. http://dx.doi.org/10.1016/j.crfs.2023.100510.

Sztucki, M. (2021). SAXSutilities: a graphical user interface for processing and analysis of Small-Angle X-ray Scattering data (1.024). http://dx.doi.org/10.5281/zenodo.5825707.

Tian, B., Wang, Z., de Campo, L., Gilbert, E. P., Dalgliesh, R. M., Velichko, E., van der Goot, A. J., & Bouwman, W. G. (2020). Small angle neutron scattering quantifies the hierarchical structure in fibrous calcium caseinate. *Food Hydrocolloids*, *106*, Article 105912. http://dx.doi.org/10.1016/j.foodhyd.2020.105912.

Ubbink, J., & Muhialdin, B. J. (2022). Protein physical state in meat analogue processing. *Current Opinion in Food Science*, *45*, Article 100822. http://dx.doi.org/10.1016/j.cofs.2022.100822.

Van Beers, R., Aernouts, B., Reis, M. M., & Saeys, W. (2017). Anisotropic light propagation in bovine muscle tissue depends on the initial fiber orientation, muscle type and wavelength. *Optics Express*, *25*(18), Article 22082. http://dx.doi.org/10.1364/oe.25.022082.

Verbeek, C. J., & Van den Berg, L. E. (2010). Extrusion processing and properties of protein-based thermoplastics. *Macromolecular Materials and Engineering*, *295*(1), 10–21. http://dx.doi.org/10.1002/mame.200900167.

Verfaillie, D., Janssen, F., Royen, G. V., & Wouters, A. G. B. (2023). A systematic study of the impact of the isoelectric precipitation process on the physical properties and protein composition of soy protein isolates. *Food Research International*, *163*, Article 112177. http://dx.doi.org/10.1016/j.foodres.2022.112177.

Verfaillie, D., Li, J., Van Droogenbroeck, B., Pannecoucque, J., Tavernier, G., Van Royen, G., & Wouters, A. G. (2024). Genetic and environmental variation in protein composition of Belgian soy determined with a novel size-exclusion chromatography method. *Journal of Food Composition and Analysis*, *130*, Article 106187. http://dx.doi.org/10.1016/j.jfca.2024.106187.

Wang, Y., Lyu, B., Fu, H., Li, J., Ji, L., Gong, H., Zhang, R., Liu, J., & Yu, H. (2023). The development process of plant-based meat alternatives: Raw material formulations and processing strategies. *Food Research International*, *167*, Article 112689. http://dx.doi.org/10.1016/j.foodres.2023.112689.

Webb, D., Li, Y., & Alavi, S. (2023). Chemical and physicochemical features of common plant proteins and their extrudates for use in plant-based meat. *Trends in Food Science and Technology*, *131*, 129–138. http://dx.doi.org/10.1016/j.tifs.2022.11.006.

Wu, B., Siglreitmeier, M., Debus, C., Schwahn, D., Cölfen, H., & Pipich, V. (2018). Ionic Dependence of Gelatin Hydrogel Architecture Explored Using Small and Very Small Angle Neutron Scattering Technique. *Macromolecular Bioscience*, *18*(6), 1–11. http://dx.doi.org/10.1002/mabi.201800018.

Yuryev, V. P., Zasypkin, D. V., Alexeyev, V. V., Genin, Y. V., Ezernitskaya, M. G., & Tolstoguzov, V. B. (1990). Structure of protein texturates obtained by thermoplastic extrusion. *Food / Nahrung*, *34*(7), 607–613. http://dx.doi.org/10.1002/food.19900340707.

Zhang, J., Chen, Q., Kaplan, D. L., & Wang, Q. (2022). High-moisture extruded protein fiber formation toward plant-based meat substitutes applications: Science, technology, and prospect. *Trends in Food Science and Technology*, *128*, 202–216. http://dx.doi.org/10.1016/j.tifs.2022.08.008.

Zink, J. I., Lutz-Bueno, V., Handschin, S., Dütsch, C., Diaz, A., Fischer, P., & Windhab, E. J. (2024). Structural and mechanical anisotropy in plant-based meat analogues. *Food Research International*, *179*, Article 113968. http://dx.doi.org/10.1016/j.foodres.2024.113968.